Experimental Methods in the Physical Sciences. Volume 35. Methods in the Physics of Porous Media. Chapter 1, Academic Press, San Diego, CA, 1-41 p., 1999.

1. DIGITAL IMAGES AND COMPUTER MODELING

Edward J. Garboczi, Dale P. Bentz, and Nicos S. Martys

National Institute of Standards and Technology
Building Materials Division
Building and Fire Research Laboratory
Gaithersburg, Maryland

Abstract

This chapter describes how digital images of porous materials can be analyzed to give information about the structure and properties of the material and the various ways 3-D digital-image-based models can be generated to help understand real porous materials.

1.1 Introduction to Porous Materials and Digital Images

Holes in objects may be desirable or undesirable. For instance, when we unwrap a piece of clothing that was ordered from an expensive mail-order catalog, and find that there are unwanted holes in it, we usually send it right back, with a more or less polite demand for a refund or an exchange. And everyone knows the effect of holes in bicycle or automobile tires. However, holes in the middle of records (remember records?) enable them to be played on a phonograph, and holes in the middle of bagels and doughnuts not only eliminate the hard-to-cook part, but also allow ease of handling by clumsy fingers. So holes can indeed sometimes be useful.

A *porous material* is simply some kind of solid material that has holes in it. The holes are also called pores. However, if asked, most people would make a distinction between a pair of socks with three holes in the toes, an empty closed cardboard box, and a household sponge. The socks and the box would not generally be considered to be porous materials, while the sponge would be. To call a material a porous material, there is usually some kind of implicit assumption of homogenization and length scale.

Attempting to state this intuitive feeling more quantitatively is difficult. We might in general say that the holes must be small enough, compared to the typical size of the piece of material that is considered, so that it is reasonable to consider the material as a mixture of solid framework and

EXPERIMENTAL METHODS IN THE PHYSICAL SCIENCES
Vol. 35
ISBN 0-12-475982-3

ISSN 1079-4042/99 $30.00

pores. Also, the holes must be distributed fairly evenly throughout the material. Therefore, if the length scale of the sample is large compared to the typical pore size, and the pores are distributed reasonably uniformly throughout the material, then the material is a porous material. We use these qualitative ideas as a working definition of most porous materials in this and later chapters.

Common porous materials, some of which are considered in the chapters of this book, include concrete [1]; paper [2]; ceramics (with natural [3] or artificially created pores [4]); clays [5]; porous semiconductors [6]; chromotography materials [7]; and natural materials such as coral, bone, sponges, rocks, and shells. Porous materials can also be reactive, such as in charcoal gasification, acid rock dissolution, catalyst deactivation [8], and concrete [1].

The purpose of this chapter is to describe a "tool kit" of mathematical and computational tools that are available for use on digital images, in general, and digital images of porous materials, in particular. These include tools for measuring geometrical and morphological quantities, tools for computing physical properties of various kinds, and tools for generating 3-D images, either from 2-D images or using models of various kinds. There are many standard review papers and monographs in this area. Sahimi's book, in particular, is a good overall reference that covers some of the same material as this chapter [9].

1.1.1 Porous Materials

Consider a sample of total volume V. Define the volume of the solid phase to be V_s, and the volume of the pore phase (the holes) to be V_p, with $V = V_s + V_p$. The volume fraction is a normalized variable that is generally more useful. The volume fraction of the pore phase is commonly called the porosity, and is denoted $\phi = V_p/V$. The solid volume fraction is then $(1 - \phi)$.

Since a porous material is a two-phase material (at least), a surface separating the pore phase from the solid phase can be defined, with its area denoted S_p. This quantity is often called the pore surface area. A normalized variable common for this quantity is called the specific surface area, $s_p = S_p/V$. Note that the dimension of $1/s_p$ is length, so that sometimes it is thought of as a length that characterizes the length scale of the pores. A simple example would be a collection of N mono-sized nonoverlapping spherical pores of radius r. The inverse of the specific surface area, $1/s_p = V/S_p$, would be $r/(3\phi)$, which is obviously a length characteristic of the pores. Other ways to form a length scale from pore space characteristics are covered later in this chapter and in other chapters of this book dealing with the transport properties of porous materials.

In thinking about the microgeometry of porous materials, a common approach is to consider them to be two-phase solid–pore composites, even though the solid phase can be heterogeneous. Properties such as elastic moduli are essentially functions of the solid phase, but are reduced and modified by the presence of the pores. If there is a fluid that fills the pore space, which can modify the dynamic elastic response, then both solid and pore characteristics must be dealt with in understanding the elastic properties [10]. Elastic moduli decrease as the porosity increases. Properties such as diffusivity and permeability are functions of pore size, shape, and connectivity and increase as the porosity increases.

The topology of the pore space of a porous material is very important in determining the properties of the material, and even in properly formulating ideas about the pore space in the first place. By topology we mean how the pores are connected, if at all. If the pores are completely isolated from each other, then clearly one can discuss the shape and size of individual pores. The left side of Fig. 1 shows an example of this case, in two dimensions, where the pores are random-size, nonoverlapping circular holes. It is clear in this case how to define the pore size distribution, a quantity that gives the number or volume of pores of a given size.

If the pores are fully connected to each other, as shown in the right side of Fig. 1, then there is really only one multiply connected "pore" in the material. The number of pores is no longer a meaningful quantity, and it becomes difficult to talk about the shape and size of the "pores." However, in this case, the idea of "throats" can be important. If the pore space in many areas is shaped like the cartoon shown in Fig. 2, then the idea of a throat shape and size can be loosely defined. The size of the "throat" limits the

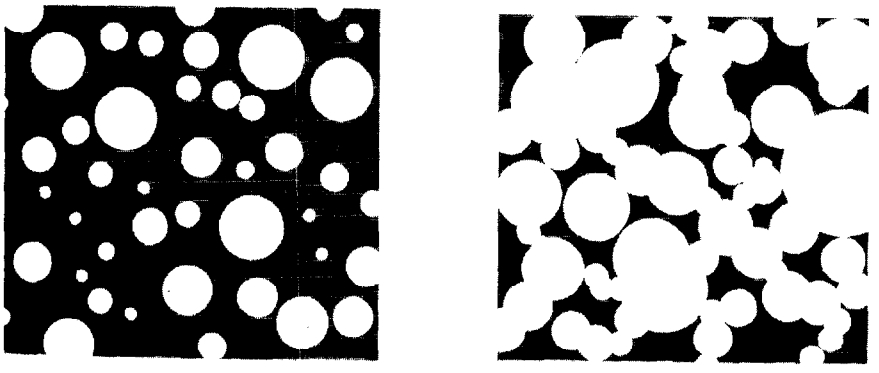

FIG. 1. Two-dimensional picture of (left) isolated circular pores and (right) connected pores (gray = solid, white = pores).

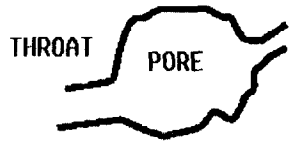

FIG. 2. Schematic picture defining a throat and pore in the pore space of a porous material.

accessibility of the larger "pore" and is then the size of importance for many properties of the material.

If there is such a throat structure, then a *pore throat size distribution*, usually but erroneously called the pore-size distribution, can be defined. Techniques such as nitrogen BET and mercury intrusion porosimetry (see Chapter 3) measure a pore throat size distribution that is convolved with the cross-sectional throat shape and the topology of the pore–throat network [7, 11]. These techniques measure an equivalent circular cross-sectional throat diameter [7, 11]. In practice, pore–throat combinations can only really be separated in terms of grossly simplified geometrical models of the pore microgeometry.

In most cases, porous materials are random materials, with random pore sizes, shapes, and topology. Because of this fact, most porous materials tend to be isotropic. This is not always the case, however. Many rocks have anisotropy built into them from how they were formed due to deposition of sediment [12]. When looking at a slice of a porous material, one must of course be aware whether the material is or is not isotropic. We assume isotropy in the remainder of this chapter.

1.1.2 Digital Images

To our eye's perception, an artist painting a watercolor or oil picture makes an analog picture, although it is actually finely divided at the scale of individual, overlapping paint pigment particles. A digital image is a collection of individual, nonoverlapping elements or pixels that have distinct intensities (gray scale or color) indicating the solid and pore phases of the material. The spatial resolution of the image indicates the size of the pixels, with high resolution meaning a small pixel is used. As the pixel size decreases, the number of pixels per unit length increases, hence the designation "high." A digital image can be a gray-scale image, where the intensity of each pixel ranges from black (0) to white (N). For many imaging systems (microscopes etc.), $N = 255$, corresponding to 8 bits of intensity resolution.

A digital image can also be a color image, where each pixel contains three values, say from 0 to 255, for red, green, and blue, forming 24 bits of color resolution. For porous materials, if the solid part is a uniform material, all a digital image requires is 1 bit per pixel, where pore is black (0) and solid is white (1), or vice versa. The importance of digital images in science, as opposed to analog paintings, is that digital images enable quantitative analysis. Old-fashioned photographs and videos also must be digitized before analysis. Modern digital cameras and scanning and transmission electron microscopes can produce digital images directly.

Usually a rectangular array of square pixels is used in two dimensions, although other shapes, such as a triangular lattice of hexagonal pixels, are also possible and can be useful for special applications [13]. Actually any area-filling collection of random shapes, on a random lattice, could be used to make a digital image. Requiring that the pixels have uniform shape restricts us to having them be a unit cell of one of the five Bravais lattices in two dimensions [14]. The further requirement that the pixels be equilateral forces the choice of square lattices of square pixels and triangular lattices of hexagonal pixels. For the rest of this chapter, we discuss only digital images made from square pixels, and in 3-D cubic lattices made up of cubic pixels.

In two dimensions, digital images at sufficient spatial resolution portray areas well. Figure 3 shows the same physical size circle, but digitized at higher and higher resolutions. The real circle is centered on the middle of a pixel. If the circles were to be centered on a pixel corner, the digitized image would look slightly different, with no significant changes. The image appears more circular as the resolution increases. Simple calculations show that when 15 or more pixels are used per circle diameter, the error in the area is always less than 1% [15].

However, the perimeter of a curved surface is usually off by a large amount, no matter what the resolution. In Fig. 3, it is easy to see that the perimeter of a digital circle P, obtained by counting pixel edges, is given by $P = 8r$, not $P = 2\pi r$ [16]. In the same way, for a 3-D digital image, where the pixels (or voxels) are now cubes, volumes are well represented at high resolutions, but the surface area of a sphere, obtained by counting pixel faces, is always approximately $6\pi r^2$, not $4\pi r^2$. These corrections must be kept in mind when trying to analyze pore surfaces based on digital images [17].

Another important issue in analyzing digital images of random porous materials is the ratio of image size to pore size. To get statistically meaningful results, the image must sample a representative area of the porous material. A more rigorous way of stating this can be formulated using the porosity. For a random porous material, the measured porosity

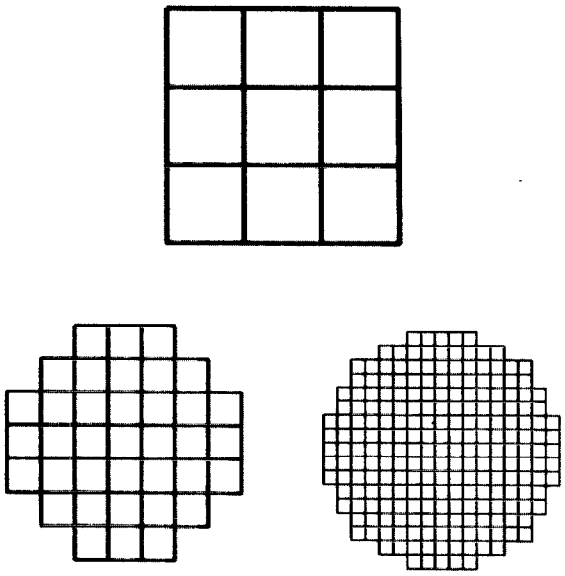

FIG. 3. Example of the effect of digital resolution on how a circle of diameter d is represented (top: pixel length = $d/3$, lower left: pixel length = $d/7$, lower right: pixel length = $d/17$).

will vary from image to image due to the randomness of the material. The smaller the image compared to the average length scale of the pores, the greater this fluctuation will be [18]. If the size of the images used is such that this fluctuation from image to image is small enough, then the image is considered to be large enough to be representative [18]. The terms "small enough" and "large enough" are defined for the application at hand. A rough rule of thumb is that the image should be 5–10 times the typical pore size.

1.2 Geometrical and Topological Analysis

Assume a digital image of a cut through a porous material has been obtained, in the form of a gray-scale image. Often the first step is to make it into a two-phase black and white image. There are many ways this can be done, based on analysis of the gray-scale histogram (distribution) of the image [19]. This histogram simply tells what fraction of the pixels have which gray-scale value. If the density of the solid phase is known, then the porosity can also be directly measured from some kind of physical bulk density measurement. If ρ_s is the solid density, and ρ is the measured

empty-pore or bulk density, then the porosity is simply $\phi = 1 - \rho/\rho_s$. A threshold gray scale can then be chosen, so that all pixels with gray levels above this threshold are white (solid) and all below are black (porosity), such that the correct porosity is achieved. Once a correct binary image has been made, further analysis can be carried out. Often, one will want to remove isolated pixels due to noise in the image acquisition process. Median filtering or other image processing algorithms can be utilized for this purpose [19].

The top left of Fig. 4 shows an example of a random image generated by convolving a Gaussian function with a random noise image (see Section

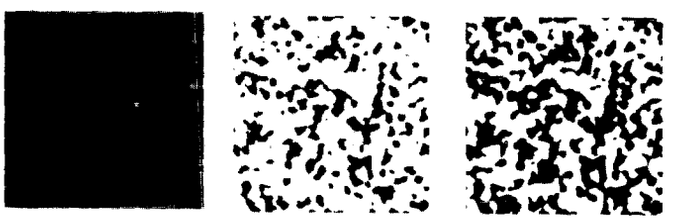

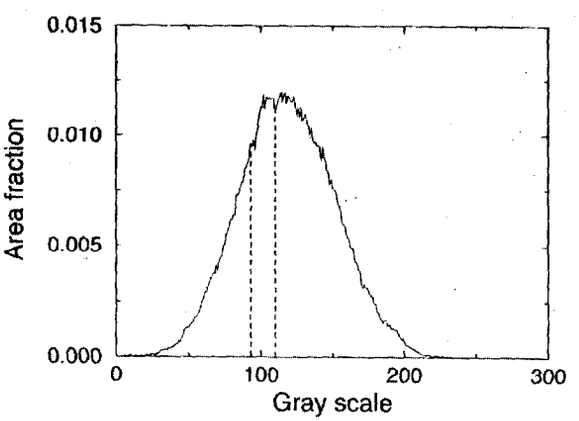

FIG. 4. Top left: an artificial gray-scale image generated from a Gaussian convolution process; middle top: the same image thresholded at a gray level of 93, so that all pixels with a gray level less than or equal to 93 are turned black and all others are turned white; black area fraction = 22%. Right top: the same image thresholded at a gray level of 110, with black area fraction of 41%. Bottom: gray-scale histogram of the original image. The y-axis is the area fraction of the image having a given gray scale, and the gray scale runs from 0 to 255. The values of 93 and 110 are marked by dashed lines.

1.5.2). The bottom of Fig. 4 shows the gray-scale histogram for this image, with dashed lines marking the gray scales of 93 and 110. In the graph, there is a single maximum at a gray scale of about 125, out of 255. Many porous material images would have two peaks in the gray-scale histogram, one for each phase. The middle top image of Fig. 4 shows the result of choosing a threshold gray level of 93, where every pixel with a gray scale lower than this is turned to black, and every other pixel is turned to white. The resulting porosity (black phase) is about 22%. If the threshold is chosen to be 110, in the top right part of Fig. 4, then the porosity turns out to be about 41%. In these 2-D sections, the pore phase is isolated and the solid phase is connected. The isolated islands of solid trapped within the pore phase are 2-D artifacts.

1.2.1 Stereology, Mathematical Morphology, and Fractal Analysis

There are several bodies of mathematical knowledge and techniques that have been developed and that are actively used to mathematically analyze and characterize the microstructure of porous materials, or indeed any material.

Stereology is the mathematical science of predicting 3-D quantities by measuring 2-D quantities. Books are available on this topic [20, 21], with many new articles produced each year. Stereology, combined with image analysis [22, 23], can be a powerful tool for inferring quantities such as ϕ and s_p that are the same in two as in three dimensions. Stereology cannot, however, analyze quantities that change between dimensions, such as percolation quantities (see Section 1.2.3). Mathematical morphology is a related and powerful tool for studying images of porous materials [24].

Another body of knowledge available for analyzing and characterizing random materials is that of fractal mathematics. Making use of the techniques of stereology, mathematical morphology, and image analysis, questions of fractal geometry [25–29] can be explored in digital images of porous materials, whether these images are 2-D or 3-D. For an object to be fractal, it must display scale invariance over a range of length scales. A given digital image must have enough resolution so that it can display a reasonable range of length scales, in order that its potential fractal character can be analyzed. A rough rule of thumb is that scale invariance must be displayed over at least one order of magnitude of length scale for an object to be considered to have fractal character. Therefore the image must contain at least that much resolution. In a digital image of a porous material, the size of the image is $L \times L$, and the pixel length is p. Clearly then we must have $L \gg 10p$, since looking at length scales too close to the digital resolution will bring in the digital "graininess," and looking at length scales too close to L will bring in finite size effects.

Assuming that the image is adequate in terms of length scales and resolution, one way to examine the possible fractal nature of an object in a digital image is to measure how the object fills Euclidean space as a function of the size of the region being examined. Such a property is characterized by the mass fractal dimension d_m. In the case of a digital image, we can count the number of pixels that are contained within a given radius. The number of points $M(r) \sim r^{d_m}$. Certainly, the range of r over which this relationship could hold would be for $p < r < L$. If the object did fill space uniformly, then $d_m = d$, the Euclidean dimension. As an example of fractal objects, objects built up in three dimensions by diffusion-limited aggregation or percolation networks at the percolation threshold have $d_m \simeq 2.54$.

Another way of determining d_m is to construct a grid that covers the digital image, of box size l. It would be easiest, in the case of a digital image, to choose l to be an integer number times p. By counting the number of boxes that included part of the object, as a function of grid spacing l, one obtains the box dimension, $d_b = d_m$, from the relation $M(l) \sim l^{-d_b}$. Once again, the range of grid spacing that would produce such a relation would be between the pixel size p and the image size L.

A surface can be rough in a way such that it can also be characterized by a fractal dimension, this time a surface fractal dimension. In a 2-D digital image, a "compass" of opening t can be used to step around the surface (perimeter) and measure its apparent length $S(t)$. If the surface fractal dimension is d_s, then $S(t) \sim t^{-d_s}$. A grid method can also be used, similar to the determination of the mass fractal dimension, which is defined for a 2-D or 3-D digital image. One counts how many grid boxes have surface within them, $S(l)$, for various grid sizes l. If the surface is fractal, then $S(l) \sim l^{-d_s}$, where d_s is again the fractal dimension of the surface.

Experimentally, one can directly determine the fractal dimension by use of small angle scattering, whether neutron or x-ray scattering. Further details can be found in Chapter 6.

For porous materials, the pore space itself, if it has pores over a wide range of length scales, can be a mass fractal [30–33]. If the pore surface is very rough, which would be the case for a high-surface-area material, then the pore surface could form a surface fractal [30–33]. Studies of fractal geometry have been carried out for rocks [26, 34], aerogels [35], and cement-based materials [36]. The transport properties of fractal pore spaces have also been studied theoretically [37, 38].

1.2.2 Correlation Functions and Bounds

Beyond the empirical characterization of pore and throat sizes, the pore geometry can be characterized in a rigorous way mathematically using

correlation functions, which can be measured using image analysis. Since they are used for bounds and the reconstruction of images, topics that are covered later in this chapter, we review them in some detail.

In 2-D, we define a function $f(i, j)$, where (i, j) indicates the location of a pixel in the $M \times N$ image, $i = 1, \ldots, M$ and $j = 1, \ldots, N$, and $f(i, j) = 0$ for solids, and $f(i, j) = 1$ for pores. Then the first-order pore correlation function is $S_1 = \langle f(i, j) \rangle = \phi$, where

$$\langle f(i, j) \rangle \equiv \frac{1}{A} \sum_{i,j} f(i, j), \tag{1}$$

and where $A = M \times N$ is the number of pixels in the image. A similar definition holds in d dimensions. The second-order correlation function, $S_2(x, y)$, is defined similarly, by

$$S_2(x, y) = \langle f(i, j) f(i + x, j + y) \rangle. \tag{2}$$

Writing the preceding equation in this way assumes that the system is translation invariant, so that only the difference vector between two pixels matters, and not the absolute location of the two pixels. If the image is also isotropic, then with $r = |(x,y)|$, $S_2(x, y) = S_2(r, \theta) = S_2(r)$, so that S_2 is a function of distance only.

The value of $S_2(r)$ carries information about how far away different parts of the microstructure still "feel" each other. When $r \to 0$, $S_2 \to \phi$, since $f(i, j)^2 = f(i, j)$. For nonzero values of r, one can think of $f(i + x, j + y)$ as a weighting probability factor for $f(i, j)$. At a given value of (i, j), such that $f(i, j) = 1$, if there is a correlation in the system up to a distance r_c, and if $r = \sqrt{x^2 + y^2} < r_c$, then $f(i + x, j + y)$ has a better than average $(> \phi)$ chance of also having the value of 1. The overall integral will still be less than ϕ, however. As $r \to \infty$, there is no causal connection between the points (i, j) and $(i + x, j + y)$, as long as there is no long-range order, so the probability associated with the pixel at $(i + x, j + y)$ being equal to unity is just ϕ, independent of (i, j). Therefore $S_2 \to \phi^2$ in this limit. A simple physical way of understanding S_2 is to think of it as the probability of finding two randomly selected points that are both in the pore space. This probability turns out to depend on the distance between the two points. Clearly, $S_2 = \phi$ when $r = 0$ and decays to the value ϕ^2 as $r \to \infty$. The decay length is a measure of the pore size. Because digital images have a finite size $(M \times N)$, the actual evaluation of the two-point correlation function can be achieved using

$$S_2(x, y) = \sum_{i=1}^{M-x} \sum_{j=1}^{N-y} \frac{f(i, j) f(i + x, j + y)}{(M - x)(N - y)}. \tag{3}$$

A simple mathematical exercise is the case of overlapping spheres, where each identical sphere is randomly placed in three dimensions without regard to any of the other spheres. The volume outside the solid spheres is the pore space. This case has been solved analytically [39, 40]. If ρ is the number of overlapping spheres per unit volume, and R is the radius of the spheres, then

$$\phi = \exp\left(-\rho\frac{4\pi R^3}{3}\right), \tag{4}$$

$$S_2(r) = \exp\left[-\rho\frac{4\pi}{3}\left(R^3 + \frac{3rR^2}{4} - \frac{r^3}{16}\right)\right] \qquad r < 2R, \tag{5}$$

$$S_2(r) = \exp\left(-\rho\frac{8\pi}{3}R^3\right) \qquad r \geqslant 2R. \tag{6}$$

Figure 5 shows $S_2(r)$ plotted as a function of r, where $R = 1$ is the radius of the spheres and $\rho = 0.29$, so that $S_2(0) = \phi \simeq 0.3$. One can see that S_2 decreases as r increases from zero, and is always monotonically decreasing. For systems where there are distinct grains, there are usually oscillations after the first large decrease in S_2. In this exactly solvable case, S_2 actually reaches the value ϕ^2, as can be seen in Eq. (6) and comparing with Eq. (4).

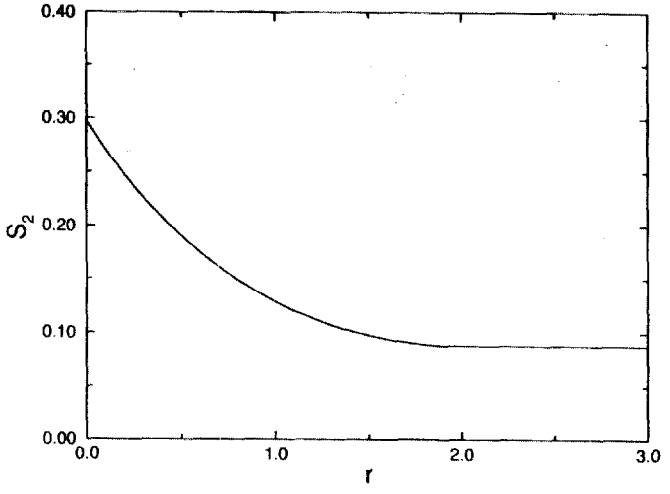

FIG. 5. Two-point correlation function for overlapping spheres (exact theoretical result). The sphere radius is $R = 1$, and the number density of spheres was 0.29, so the volume fraction of pore space ϕ, which is the space surrounding the solid spheres, is approximately 0.3.

For any random isotropic pore space with smooth surfaces, the slope of the two-point correlation function at $r = 0$ is given exactly by [41–43]

$$\frac{\partial S_2}{\partial r}|_{r\to 0} = \frac{-S_p}{4V} = -4s_p. \tag{7}$$

Therefore S_2 is always a decreasing function of r for small r, because of this negative initial slope.

Note that $S_2(r)$ also contains additional information when fractal geometry is present [29]. In the case where the material phase considered is a mass fractal, $S_2(r) \sim r^{d_m - 3}$ when r is in the fractal limit (less than the image size and greater than the pixel size), where d_m is the mass fractal dimension (see Section 1.2.1).

When the material phase is Euclidean, but its surface is fractal, with dimension d_s, the small r limit is given in terms of the surface fractal dimension: $S_2(r) \sim \phi B r^{3-d_s} + \cdots$, where B is a constant [29]. When the material phase is a mass fractal with a fractal surface, then other mathematical forms must be considered [29].

Higher-order correlation functions are defined similarly. Although in practice, two-point functions are most used, three-point functions are fairly common, but correlations past three-point are rarely used. For an isotropic translationally invariant material, the three-point correlation function, S_3, is a function of three variables, r_1, r_2, and θ where these can be thought of as defining a triangle with two sides of length of r_1 and r_2, with θ being the angle between these two sides. Then $S_3(r_1, r_2, \theta)$ is the probability of finding the three vertices of this triangle all in the pore phase [39].

When computing correlation functions from digital images, it is important to correctly handle certain technical issues such as converting to polar coordinates, especially at small r, and to consider the limitations of digital images, such as digitizing curved surfaces, which were mentioned earlier. References [40, 44, 45] give explanations of the methods that must be used, the pitfalls of which to be wary, and the sources and magnitudes of possible errors.

Other than characterizing pore geometry, one of the principal uses of correlation functions is in the area of computing bounds for the effective properties of composite materials [46, 47]. Bounds are analytical formulas that, for some particular property such as elastic moduli or electrical conductivity, give the upper and lower limits for what the effective composite property can be.

Bounds are classified by their order. An nth-order bound usually includes information from the nth order correlation function [46, 47]. Of course, if there are more than two phases, there will be more than one nth-order correlation function. However, the second-order bounds for elastic moduli and

electrical–thermal conductivity, commonly called the Hashin–Strichkman bounds [47], are unusual in that they do not explicitly contain information from S_2, the second-order correlation function, other than $S_2(0) = \phi$. But the third-order bounds for these properties do have parameters computed from S_3. The first-order bounds are simply the parallel (Voigt) upper bound and series (Reuss) lower bounds, for which the phases are arranged in a parallel or series microstructure. These use the same information as the second-order bounds, the volume fraction and properties of each phase, but are wider apart than the Hashin–Strichkman bounds.

As bounds incorporate higher and higher correlation functions, they are known to become tighter and tighter, increasing their usefulness at the expense of a great increase of computational difficulty. In fact, it is known that the isotropic and anisotropic electrical conductivity [46,48] and isotropic elastic moduli [49] of a random isotropic two-phase composite can be written down exactly in powers of the difference of the properties of the two phases. The coefficients in the power series are functions of all the correlation functions of any order for the composite. So, in general, the properties of a porous material will depend on all order correlation functions.

Bounds are most useful for composite materials where none of the phases have zero properties. They are less useful for air-filled porous materials. This is because in the array of nth-order bounds, the lower bound always has something of a series character and the upper bound always has something of a parallel character. For air-filled porous materials, this means that the lower bound is always close to zero, because air approximates a zero-property phase. So there is really only an upper bound for air-filled porous materials, which may or may not be very close to the actual effective properties. For a liquid-filled porous media, a meaningful lower bound can exist. However, for elastic properties, a zero shear modulus in the liquid phase causes both the lower shear modulus and Young's modulus bounds to be zero.

There has been much work in the past decade or so on bounding the permeability, which is a more difficult problem than that of bounding the effective electrical conductivity or elastic moduli [46, 50–53]. Permeability is different from quantities like electrical conductivity and elastic moduli. The conductivity, for example, is defined at every point of the material, and the overall effective conductivity is found by solving Laplace's equation [Eq. (9)], for the composite and averaging over this solution and the microscopic conductivities. However, there is no microscopic permeability, because permeability cannot be defined at a point, even in the pore space, but is defined instead by averaging over solutions of the Navier–Stokes equations in a porous material.

1.2.3 Pore Connectivity

Assessing the connectivity of any phase is simple in a digital image of a porous material. Usually, we want to know this for the pore phase, as the solid phase must be connected to have mechanical integrity of the sample. A simple method to use on a digital image is called a "burning algorithm" [54, 55]. In two dimensions, only one phase at a time in a porous material can be percolated [54, 56]. In three dimensions, several phases can simultaneously percolate. This fact reduces, but does not eliminate, the usefulness of the burning algorithm in two dimensions.

The burning algorithm is a way of identifying all members of a cluster of connected pixels that span the image. Starting on one side of an image, "burn" one pore pixel by setting its gray scale to another number that is not in the existing range; for example, not in the range 0–255. Then any pore pixel that touches this pixel is also set to the same number. Continue this process until there are no more "unburned" pore pixels left that are touching the last burned pixels. The process is similar to classifying all pixels of a certain gray value as being combustible, and then touching a match to one of them. If the "fire" burns from one side of the image to the opposite side, then the burned pixels are said to form a spanning cluster, or percolate. This process can be repeated by starting the fire at any unburned pixel to identify all connected clusters, and all nonspanning clusters as well. This is an efficient way to determine if the pore space percolates through the digital image.

In performing the burning algorithm, one issue to consider is which pixels constitute a neighboring pixel for propagation of the "fire." The most common case is to consider the immediate nearest neighbors (4 in two dimensions, 6 in three dimensions). Alternately, the second nearest neighbors (4 in two dimensions), or the second and third nearest neighbors (20 in three dimensions) can also be considered. The connectivity of a phase in a digital image with square or cubic pixels has this degree of uncertainty. We note, however, that using only the first nearest neighbors in two dimensions resulted in good agreement of percolation thresholds, determined on digital images, with their continuum counterparts [15]. Different numerical techniques for discretizing continuum equations on a digital image have natural definitions of connectivity connected with them, as we see in the next section.

It is important to note that percolation thresholds are usually larger in two than in three dimensions. For instance, if one carries out site percolation on a square lattice digital image, considering only nearest neighbor connections, where a random fraction x of the pixels are white and $(1 - x)$ are black, then the white pixels will percolate only when $x \geq x_c$, where $x_c = 0.59$

in two dimensions, but $x_c = 0.31$ in a 3-D simple cubic lattice [56]. If the pore space of a real material followed these site percolation statistics, and had a porosity of 35%, it would have a percolated pore space, but, seen in the microscope, a 2-D slice would appear to have a disconnected pore space, as a porosity of 35% is much less than $x_c = 0.59$. Thus it is incorrect to study 3-D percolation quantities using 2-D images. Stereology breaks down in this instance, as the connectivity in three dimensions and two dimensions is fundamentally different. Real pore spaces, which generally have different kinds of percolation statistics, will also show difference. Since the connectivity of the pore space has a critical influence on transport properties such as permeability [57], its quantification can be critical for understanding microstructure–transport property relationships.

1.3 Computing Material Properties from Images

By the fact that it is already divided into pixels, a digital image is easily adapted to discrete computational methods, such as finite difference, finite element, and lattice Boltzmann methods. Since there is an underlying lattice, any known algorithm for lattice problems can be applied. A manual available through the Internet describes a collection of various programs [58] that apply finite difference and finite element methods to any 2-D or 3-D digital images. These programs can be used to compute a variety of material properties to compare with experiment. Later in the chapter we discuss how the different methods can be applied to two-phase pore–solid images, representing materials in which either the solid or the pores have a uniform property, and the other is zero. An example of the case where the solid is insulating and the pores are filled with a conductive fluid is Vycor™ glass filled with a liquid metal [59]. On the other hand, we could have a conducting granular backbone and insulating pores [60]. Similarly for elastic properties, the solid is assumed to have a uniform elastic modulus tensor, while the pores have zero elastic modulus. For hydraulic permeability, the fluid can only flow in the pores.

Both finite element and finite difference methods are simply means of converting partial differential equations into a set of approximate algebraic equations. At this point, however, it is worth noting some of the differences between the finite element and finite difference methods discussed in this chapter. The linear electrical conduction and linear elasticity problems can be formulated either directly as a set of linear partial differential equations or, indirectly, as an energy functional of partial derivatives that obeys a variational principle. We present finite difference methods for the electrical conduction case, and finite element methods for the elasticity case. The full

Navier–Stokes equations are nonlinear and do not have an associated variational principle [61]. The linearized forms of these equations, the Stokes equations, do have a variational formulation [62]. However, we present only finite difference methods for the fluid flow case.

In the various methods presented in this chapter, there also can be differences in node placement. In a digital image, we want to use no more than one node per pixel, if possible, to conserve memory. Philosophically, this is also desirable since having more than one node per pixel would seem to imply that more information is available than is really present in the pixel structure. In a digital image, there are as many pixel corners as there are pixels or pixel centers, so a reasonable choice of node location would be either pixel corners or pixel centers. Of course, just as one can use any coordinate system to solve a physical problem, the node placement can be arbitrary as well. However, for example, one would not choose parabolic coordinates to solve a problem involving the surface of an ellipsoid, because ellipsoidal coordinates result in algebra that is much easier to work with than parabolic coordinates in this case. In the same way, for the finite difference and finite element methods, certain ways of choosing the node placement result in much simpler equations.

1.3.1 Steady-State Conduction

The important problem of steady-state conduction is a good case in which to see the differences between finite difference and finite element methods. The partial differential equation to solve is

$$\nabla \cdot \vec{j} = 0, \tag{8}$$

where $\vec{j} = \sigma \vec{E}$ is the current flux, and $\vec{E} = -\nabla V$, with V being the potential of the problem, and σ the local conductivity. Inside a constant conductivity material phase, this equation becomes the same as Laplace's equation,

$$\nabla^2 V = 0. \tag{9}$$

Between phases with different values of σ, the normal flux, along with the potential, must be continuous at a phase boundary. The energy functional that obeys a variational principle is given as

$$\frac{1}{2}\int \vec{j} \cdot \vec{E} d^3 r. \tag{10}$$

When this functional is extremized, the preceding differential equation results, with the correct boundary conditions.

In a digital image, all phase boundaries are also pixel boundaries. Having a square array (in two dimensions) or a cubic array (in three dimensions)

of pixels means that locally all boundaries are oriented in one of the principal directions. Since in a direct finite difference formulation of the partial derivatives of the problem, the derivatives are thought of as being between the nodes, it makes sense in the finite difference formulation to place the nodes at pixel centers, so that the boundaries are always located exactly between nodes. To get a finite difference form of Eq. (8), we simply expand the partial derivatives of the potential around the center of the pixel of interest, pixel m, to obtain

$$\Sigma_j S_{m,j}(V_j - V_m) = 0, \tag{11}$$

where $S_{m,j}$ is the conductance connecting pixels m and j, and V_m is the voltage at pixel m. For a porous two-phase material, if pixels m and j are both conductors, then $S_{m,j}$ is just the conductance of one conducting pixel. Otherwise, $S_{m,j} = 0$. For an electrolyte-filled rock, in the case of electrical conductivity, the pore phase is the conductor and the solid phase is the insulator. In the case of steady-state thermal conduction of a rock with empty pores, the solid phase becomes the conductor and the pore phase becomes the insulator. When there are two types of conductors, the finite difference formulation implies that $S_{m,j}$ becomes a series combination of the conductances of one-half of pixel m and one-half of pixel j [58, 63]. Figure 6 shows a piece of a finite difference network superimposed on a random image, where the gray pixels are conducting and the white pixels are insulating. The bonds indicate conducting connections between nodes.

A finite element solution of Laplace's equation can also be generated using the variational principle that the correct solution gives the minimum energy dissipated, averaged over the random structure [58]. Now the finite

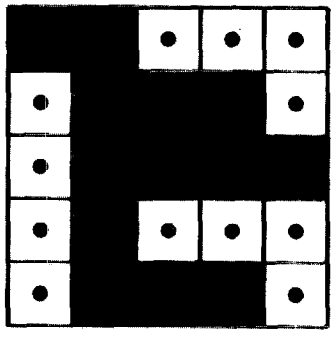

FIG. 6. Finite difference grid for a piece of a digital image. The gray area has nonzero conductivity, and the white area is insulating. The nodes are at pixel centers, and the lines connecting the nodes indicate mathematical "bonds."

element nodes are placed on the corners of the pixels, with the voltages given at the pixel corners instead of at the pixel centers. The voltage at the interior of the pixel is found by linear interpolation of the corner voltages. Equation (10) is then approximately computed, pixel by pixel, by integrating over each pixel and then summing over all pixels. This converts the energy functional into a quadratic form that involves the nodal voltages. This functional is minimized to solve for the nodal voltages and the approximate solution to the conduction problem. In many cases, the finite difference method is simpler and gives results that are just as accurate. For the case where two or more phases have a nonzero conductivity, sometimes the finite element method can be more accurate [58]. Figure 7 shows some of the finite element nodes superimposed on the same digital image as was shown in Fig. 6. Again, the gray phase is the conducting phase.

As mentioned earlier, the connectivity of a digital image can vary when different sets of neighbors are defined to be connected [64]. This can affect the result of computations. In the finite difference cases already described, the only mathematical connections are between nearest neighbor pixels. In the finite element method, however, since the nodes are at the corners of a pixel, and all the nodes on the corners of a given pixel are mathematically connected in the quadratic form, the result is that in two dimensions, each node is mathematically connected to nine different nodes, itself and its four nearest and four second nearest neighbors, which are the nodes in the corners of the four pixels that share a corner. In three dimensions, each node is mathematically connected to 26 other nodes plus itself. Therefore a conducting structure that is physically made up of pixels connected only by corners would be connected electrically when using finite elements but

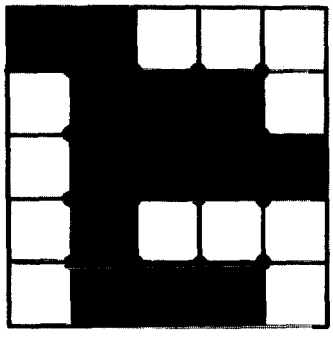

FIG. 7. Finite element grid for the same digital image as shown in Fig. 6. The nodes are now at pixel corners, where variables such as voltages and elastic displacements are evaluated. Both gray and white regions can have nonzero elastic moduli.

disconnected electrically when using finite differences. There is not much difference when the image resolution is high enough so that even the smallest feature is made up of many pixels. However, for low-resolution digital images, there can be a difference between the answer that these two methods give, with generally no way of distinguishing which is preferred. If the real pixel-to-pixel connections are defined beforehand in some way, so that only certain neighbors are "really" connected, this will give insight into which method to use. Otherwise, the choice is arbitary. However, exact solutions for various nontrivial systems can be used to check the accuracy of these different methods [58], in some cases distinguishing between them in a quantitative way.

1.3.2 Fluid Flow

Fluid flow in porous materials is of great interest for many practical reasons, including the service life of building materials, petroleum recovery, waste containment, catalysis, and filtering [7, 26, 65]. The continuum equation for calculating flow properties is the Navier–Stokes equation [65]. The Stokes equation is the slow-flow linearized version of the full Navier–Stokes equations. For flow through porous materials, in almost all cases, one is just interested in this slow-flow limit. The Stokes equation, in the steady-state limit, is given by [65]

$$\nabla^2 \vec{v}(\vec{r}) = \frac{1}{\mu} \nabla P(\vec{r}), \tag{12}$$

where $\vec{v}(\vec{r})$ is the fluid velocity at the point $\vec{r}$, $P(\vec{r})$ is the pressure at the point $\vec{r}$, and μ is the fluid viscosity. For incompressible fluids, an additional condition,

$$\nabla \cdot \vec{v}(\vec{r}) = 0, \tag{13}$$

applies.

There are many different ways to solve the Stokes equations [66], including both the finite difference and finite element methods. One way of solving the Stokes equation that is well adapted to a digital image uses a "marker-and-cell" (MAC) mesh [66]. Figure 8 shows the same image as in Figs. 6 and 7, where gray is the pore phase through which the fluid flows. The nodes indicate where the pressures are determined, and arrows show where the fluid velocities are determined, in the middle of pixel sides [16]. All fluid velocities right at a gray–white (pore–solid) boundary are set to zero, so no arrows are shown at these points in Fig. 8. This algorithm is similarly constructed in three dimensions [57].

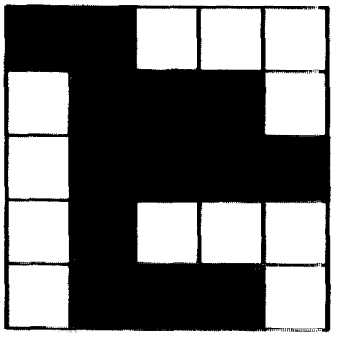

FIG. 8. Part of the MAC mesh for the same digital image as was used in Figs. 6 and 7. The pressure is evaluated at the nodes, and the fluid velocities are evaluated at the arrow tips, at pixel boundaries. The gray area is pore space and contains fluid, and the white areas are solid. Fluid velocities are forced to be zero (no arrows shown) at fluid–solid boundaries.

Darcy's law [65] is found to describe macroscopic flow through porous media:

$$\vec{v} = \langle \vec{v}(\vec{r}) \rangle = \frac{k\Delta P}{\mu L}, \tag{14}$$

where k, the permeability, has dimensions of length squared, $\vec{v}$ is the average fluid velocity in the entire volume of the sample (not just the pores), and ΔP is the pressure drop over the sample length L. Darcy's law is a macroscopic equation, obtainable from the Stokes equation [67], which treats the porous material as a homogeneous material defined by a certain bulk resistance to fluid flow through it. Darcy's law is mathematically analogous to Ohm's law, with μ/k playing the role of the resistivity.

Since permeability has units of length squared, and the conductivity, normalized by the conductivity of the conducting phase, is something like a dimensionless tortuosity, there have been many attempts to generate a length scale from the pore space that can relate the two quantities. The most widely used of these length scales are based on the specific surface area [65], an electrically weighted specific surface area that comes from solutions of Laplace's equation in the conducting pore phase [68] and a length scale based on mercury injection [69]. A common idea has been to find a length scale that correctly weights the parts of the pore space where the fluid actually goes. These length scales are all reviewed and compared on the same set of digital images in Ref. [16].

1.3.3 Linear Elasticity

The linear elastic properties of porous media can be computed by finite difference or a finite element methods applied to digital images. Expressed in terms of the elastic vector displacement, $\vec{u}(\vec{r})$, the Poisson's ratio ν of an isotropic solid, and ignoring the effect of gravity, the vector equation to be solved is [70]

$$(1 - 2\nu)\nabla^2\vec{u} + \vec{\nabla}(\vec{\nabla}\cdot\vec{u}) = 0. \tag{15}$$

For a two-phase image (solid and pores), where the solid has a uniform elastic moduli tensor and both elastic moduli are zero in the pore space, a finite difference approach can be used [71]. The boundary condition of zero normal force at a solid–pore boundary is automatically satisfied in the finite difference formulation [71]. When there are two or more kinds of solid materials, or when the pore space is filled with an incompressible fluid, it is difficult to incorporate into a finite difference formulation the boundary conditions of continuity of elastic displacement and normal stress at boundaries between different elastic moduli regions. It is easier to use a finite element formulation, which makes use of the variational principle that the correct displacement solution minimizes the elastic energy under an applied strain [58, 72]. The finite difference method would use a grid just like that shown in Fig. 6 with elastic displacements determined at the nodes in the pixel centers, while the finite element method would use a grid like that in Fig. 7 with elastic displacements determined at the pixel corners. In the displacement formulation [73] of the finite element method, continuity of displacement is satisfied automatically, but continuity of normal stresses is only approximate.

Figure 9 shows the component σ_{xx} of the computed stress tensor throughout the 22% porosity microstructure shown in Fig. 4, where the solid (white) phase was fully connected with a Poisson ratio of 0.2 and a Young's modulus of 1.0 in arbitrary units. A horizontal strain (ε_{xx}) of 0.01 has been applied across the sample. Figure 9 was obtained using a finite element method [58]. The brighter the gray scale, the higher the stress. The pores are shown in black, and the compressed regions are shown in an uniform dark gray. Because of the randomness of the porous material, even though the average strain is tensile, there will still be regions of compressive stress. Notice that the areas of compressive stress are always near a pore. On the other hand, the areas of high tensile stress are almost always at the bottom or top of a pore, due to the stress concentration effects of a cavity in a tensile strain field [74]. Figure 10 shows the corresponding stress histogram. The area under the histogram has been adjusted to be 1, rather than 1 − porosity, because the zero stresses in the (empty) pores have been

FIG. 9. The horizontal tensile stresses (σ_{xx}) for the 22% porosity microstructure shown in Fig. 4, where the solid phase (white in Fig. 4) has a Poisson's ratio of 0.2. The brightness is proportional to the tensile stress magnitude, with pores shown in black. Areas of compressive stress are in dark gray.

ignored. The effective Young's modulus of this porous material was about $\frac{1}{3}$. The effective moduli are easily determined by computing the average stress tensor and then extracting the effective moduli using the applied strain and well-known composite theory [46, 47]. Reference [75] describes a successful comparison with experiment using the finite element elastic technique to compute the effective elastic and shrinkage properties of porous Vycor™ glass.

1.3.4 Nonwetting Fluid Injection

A simple simulation of injection of a nonwetting fluid has been developed in two dimensions [76] and three dimensions [77, 78]. The results can be compared with mercury porosimetry experiments. The idea is to apply the "equivalent sphere" concept to digital images in the following way [79]. For

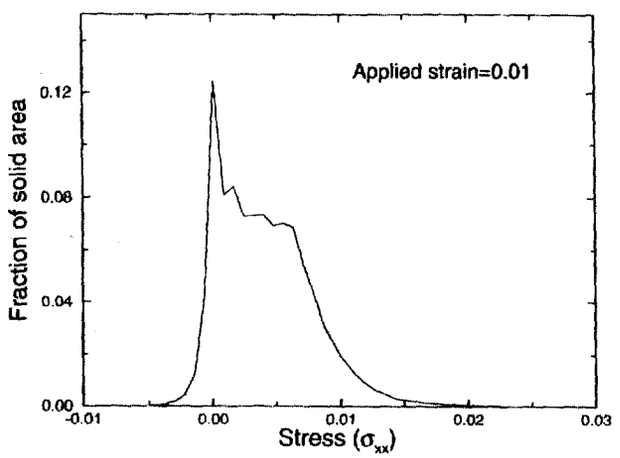

FIG. 10. Showing a stress histogram for the computed stress fields shown in Fig. 9. The applied strain was 0.01, and Young's modulus of the solid phase was 1.0 in arbitrary units.

a given injection pressure P, there is a corresponding pore radius R, $P \sim 1/R$. In three dimensions, a sphere with radius R is put into the image from the outside, and moved around to cover as much volume as possible without overlapping the solid. As the injection pressure is increased, the size of the sphere is decreased. The amount of additional volume swept out at each progressively smaller value of R is the pore space assigned to that pore size or to its equivalent pressure [11, 76], just as in mercury injection porosimetry. In two dimensions, this technique is fairly accurate, as there is only one radius of curvature for a meniscus, and it is reasonably approximated by a circular arc. In three dimensions, however, there are two principal radii of curvature at any point on the surface of a liquid meniscus. Thus using a sphere to simulate the meniscus is much less reliable. Mathematical morphology techniques can also be utilized in simulating these processes in porous media [80].

Figure 11 shows a simulation of mercury intrusion (gray) in a material in which the solid frame (white) is made up of randomly placed, rigid overlapping monosize circles (white) [76]. The uninvaded pores are in black. The left-hand side is for a lower pressure, where only surface intrusion has occurred. The right-hand side shows the intrusion that occurs at higher injection pressure, where the nonwetting fluid can get into smaller pores. Clearly, there are large pores that are not invaded because they are only accessible by small throats. This is the well-known "ink bottle" effect [81].

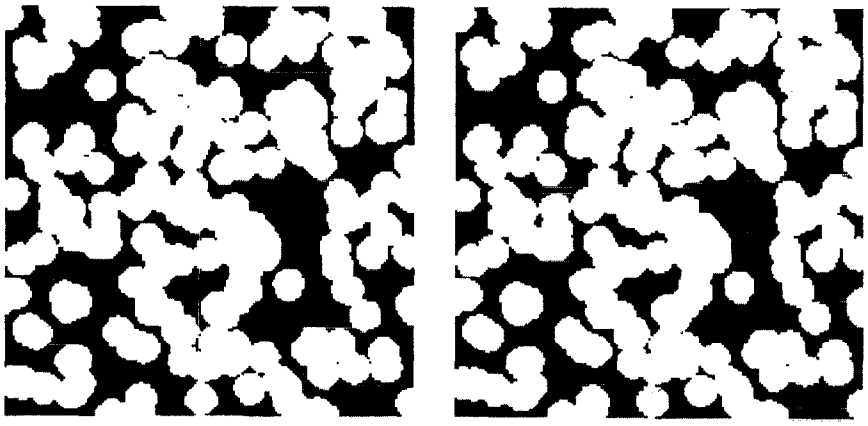

FIG. 11. Example of the intrusion of a nonwetting fluid (gray) into the empty pore space (black) around the solid (fixed) circles (white). Left: low-pressure intrusion; right: high-pressure intrusion.

Moisture absorption is important in the study and use of porous materials in atmospheric conditions (see Chapter 3). A typical quantity measured is the sorption isotherm, which is the amount of moisture absorbed as a function of the partial pressure of the absorbing vapor, at a fixed temperature. A simple variation of the mercury injection simulation can be made so as to simulate the moisture absorption–desorption processes in any digital image of a porous material in two or three dimensions [75, 78, 80].

1.3.5 Cellular Automaton Fluid Methods

Two additional computational fluid dynamics algorithms, originally based on cellular automaton ideas, that are alternative to the direct finite difference solution of the Stokes equation are the lattice gas [82] and lattice Boltzmann methods [82–84], as applied to porous materials. These methods, in contrast to the finite difference and finite element methods, do not directly discretize the continuum Navier–Stokes equations but rather operate at the "fluid particle" level.

The lattice gas method tracks the motion of particles moving on a lattice that are subject to collison rules that guarantee conservation of mass and momentum. Macroscopic variables such as density and flow velocity are obtained from statistical analysis of the particle motions.

In contrast, the lattice Boltzmann method solves for the time evolution of

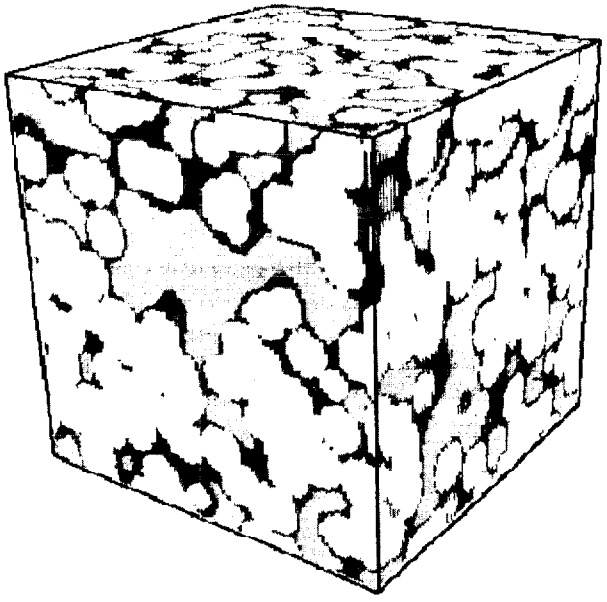

FIG. 12. A 3-D lattice Boltzmann simulation of the phase separation of two immiscible fluids in a porous material, where one fluid wets the solid phase (solid = white, dark gray = wetting fluid) and the other does not (light gray = nonwetting fluid).

the fluid particle velocity distribution function, which evolves due to the "collision" of fluid particles. Quantities such as fluid density and velocity can be easily obtained from moments of the distribution function. The method can be applied to any digital image of a porous material, and the resulting fluid behavior proves to satisfy the Navier Stokes equations. Due to ease of implementation, the lattice Boltzmann method is much more frequently used than the lattice gas method.

For a given digital image and the simple problem of saturated single-fluid flow driven by a small pressure gradient, it may be easier to use a finite difference code for the Stokes equations. However, the lattice Boltzmann method is much more useful in treating multiphase flow problems because interfacial forces between liquid, gas, and solid phases can be more easily incorporated. Thus flow and wetting properties in partially saturated porous materials can be obtained in two or three dimensions [82–84].

One example is shown in Fig. 12, which depicts a 3-D computation of the phase separation of two immiscible fluids inside a model porous material. One fluid (dark gray) wets the solid (white), and one does not (light gray).

The simulation starts with the fluids homogeneously mixed and present everywhere in the pore space. The lattice Boltzmann algorithm causes the two fluids to phase separate, with the wetting fluid preferentially moving to the solid surface.

1.4 Creating Isotropic 3-D Structures from 2-D Images

There are various ways to obtain 3-D images from 2-D images. Experimentally, 3-D images may be built up from a set of 2-D serial sections [85]. This is a tedious and time-consuming task, even with an automated system. X-ray tomography offers one possibility for rapidly obtaining a 3-D image of a microstructure. Resolution limits of several micrometers per pixel can be achieved. This is adequate for many porous materials [86–88] (see Chapter 8). Sample sizes of a few millimeters or centimeters can be accommodated, depending on the needed resolution. The acquisition and processing of such images are rapid because no physical slicing of the sample is involved. The rest of this section describes a method for generating 3-D images from 2-D images in cases where 3-D images are not readily or directly obtainable.

1.4.1 Quiblier Method

An interesting theoretical approach to generating 3-D images is to generate a representative 3-D porous medium from a single 2-D view of the system, such as that provided by a conventional micrograph illustrating the pore system. Based on the work of Joshi [89], Quiblier developed a computational technique for creating a 3-D microstructure based on two-point correlation function (S_1) analysis of a 2-D image [90]. The main principle is that a 3-D image is produced that has the same one-point and two-point correlation functions as did the real material, as determined in the 2-D image. In essence, S_2 obtained from the 2-D image is introduced into a 3-D image by convoluting an initial image consisting of Gaussian noise. The resulting image is then filtered so as to have the same S_2 as the original image. This involves solving a large number of nonlinear equations [90]. In his original paper, Quiblier performed some stress calculations on a slice of the generated 3-D medium. Adler et al. [91] utilized this technique to generate 3-D images of Fontainebleau sandstones. They computed permeabilities [91] and conductivities [92], but the results were consistently lower than measurements on real samples. This is probably due to differences in the pore space connectivity since S_2 does not contain such information. The evidence of this weakness is the difference in percolation thresholds. Pores in sandstone are known to become disconnected at a few

percent porosity, but the 3-D generated images tend to have percolation thresholds near 10% porosity [91].

1.4.2 Simplified Method

A simplified version of the approach outlined by Quiblier has been developed that modifies the generated 3-D structure based on analysis of the hydraulic radius of the pore space [93, 94]. Transport properties such as permeability and conductivity and the critical pore diameter can be computed to evaluate the merit of the generated 3-D microstructure. An example in Fig. 13 shows the original scanning electron micrograph (SEM) of a porous clinker brick, along with a thresholded and two-phase view of solid plus pores [94]. In the modified generation procedure, S_2 is calculated using Fig. 13 (right) and then used to generate a 3-D microstructure. The value of s_p for this structure is not equal to the original value. The hydraulic radius of the 3-D structure is then modified so as to force its value of s_p to match that of the real image [93], which also makes the two-point correlation function approximately match the real one as well. A 3-D view of the final generated brick microstructure is shown in Fig. 14, with the pores in black. As pointed out earlier in Section 1.2.3, while the pores appear discontinuous in the 2-D image, they are actually connected in the generated 3-D image.

1.4.3 Limitations of 2-D to 3-D Image Generation Methods

There are advantages and drawbacks to generating 3-D porous microstructures from 2-D images. If the geometrical characteristics of a porous

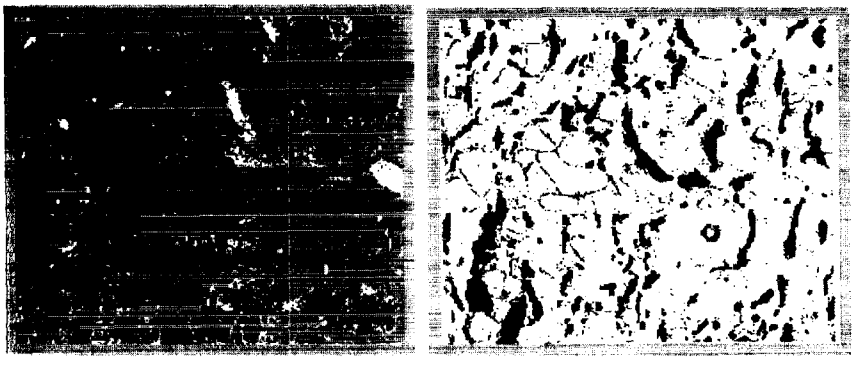

FIG. 13. A starting 2-D SEM image of the clinker brick (left) and a thresholded binary image showing pore regions in black (right). Each image is about 500 μm wide.

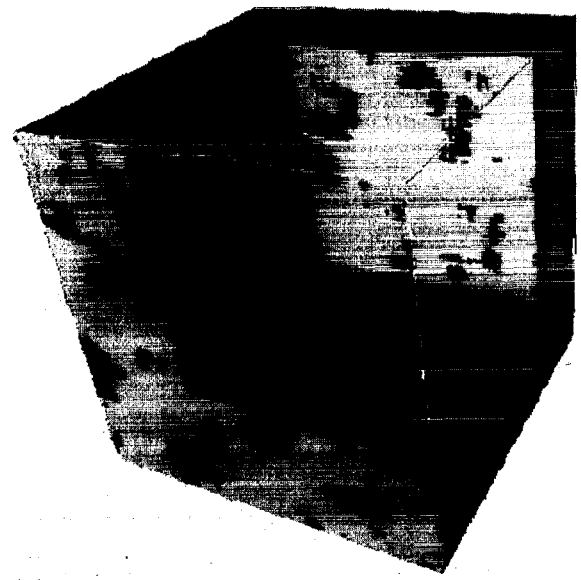

FIG. 14. A cutaway view of a 3-D reconstructed image of the clinker brick with the same porosity (black) as the original 2-D image.

material are well captured by S_2, then the generated image can be used to compute other properties as well. If the geometrical information in $S_3, S_4, \ldots$ or the connectivity of the pore space is important for the computed properties, then there is no substitute for the real 3-D image [75].

1.5 Microstructure Models in Three Dimensions

Besides using digital images of real materials to compute their various physical properties, it is often useful to construct artificial models to elucidate the essential physics. There are three broad classes of 3-D models for porous materials.

The first kind of model is called a *percolation-type* model. Here, one builds up a structure using randomly or regularly deposited shapes of various kinds within a finite imaging field; for example, overlapping ellipsoids, lattices of overlapping spheres, or a random or regular lattice of tubes. The result is a 3-D structure that bears some similarities to real materials and is easy to generate on a computer. They can give real insight into parameters such as percolation thresholds, transport properties, and their interrelation-

ships. However, the values of parameters in the models are not to be compared with real materials.

The second type of model is usually based on smoothing of a random noise image. A random noise image is first created, and then mathematical operations are carried out to transform it into something that resembles a real material. There is no attempt to simulate the actual physical and chemical processes that create the porous material. Cellular automaton methods can also be used to generate images that look like the "real thing" without attempting to duplicate the actual physics and chemistry [95].

The third kind of model is a microstructure development model that tries to simulate the actual processes by which the material is made. Examples, to be discussed further later in the chapter, include models for the formation of cement-based materials, sintered ceramic materials, and sedimentary rocks. These kinds of models are usually harder to create than the first two kinds, requiring insights into the physical and chemical processes, and the algorithms are more complicated. However, their output can be compared directly to images of the real materials and their measured properties. An image of the actual starting materials, as we shall see, can often be used as the starting point for these kinds of models. The outcome of a microstructure development model can be visually compared to images of the real material. At the crudest level, this is the "duck" test: If it looks like a duck, then it is a duck. However, using the tools developed in Sections 1.2 and 1.3, more quantitative tests can be conducted; for example, various correlation functions can be compared and other properties can be computed and compared against experimental data. Good agreement validates the assumed physical and chemical processes contained in the model.

1.5.1 Percolation-type Models

Percolation theory is a well-studied topic, with many excellent reviews [54, 56, 96–98]. The early studies of percolative structures and their effects on bulk physical properties were made on random lattice structures, thus making them relevant to structures seen in digital images, which are typically square or cubic lattice structures. A digital image approximates a continuum structure when the geometric features of interest each occupy many pixels. In this sense, a useful digital image is a lattice structure with spatial correlations among the pixels [99, 100].

There has been less, but still substantial work, on generating 3-D continuum models using continuum objects placed at random or regular positions within the image frame. Many references can be found in the reviews cited earlier. One example is to build microstructures out of overlapping, randomly placed and oriented ellipsoids [101]. Figure 15

shows a 2-D section of such a 3-D model. The prolate ellipsoids used were of the same size with an aspect ratio of 10. The volume fraction of ellipsoïds in Fig. 15 is approximately 7%. Even though in the image, the ellipsoids appear to be mostly isolated, over half of them are connected in three dimensions and form a spanning cluster. Note that a similar model with ellipses in two dimensions having the same aspect ratio would percolate at an area fraction of about 30% [102].

Building continuum models with other objects in three dimensions was reviewed by Balberg [103] and they are relevant to real processes. Cubes were used to study percolation processes in the combustion of carbon [104], and regular lattice packings of spheres have been used to study capillary condensation hysteresis loops [105]. A regular lattice packing of spheres that can consequently grow and overlap, called the grain consolidation model, has been used to gain insight into transport processes in sedimentary

FIG. 15. Slice through a 3-D model of overlapping prolate ellipsoids (white) having an aspect ratio of 10. The volume fraction of ellipsoids is 7%.

rocks [106]. Two-dimensional lattices of disks that can rub against each other have been used to simulate the elastic properties of sandstone [107]. Other discussions of percolative-type models can be found in Ref. [46].

A subset of this approach, mostly used for simulating fluid flow in porous materials, is the use of tube networks, both regular [108] and random [109]. In some sense, this is similar to using discrete conductor networks to solve the continuum Laplace equation [100]. However, setting up a finite difference solution of the continuum Stokes equation in a porous material does not result mathematically in equations that resemble those for a network of tubes. Nevertheless, a great deal can be found about flow in porous materials from this approach [110]. More details can be found in Chapter 2.

1.5.2 Artificial Image Models

The second set of models are what we call artificial image models. In Section 1.4, the measured two-point correlation function, S_2, measured on a 2-D digital image of a real material, was used to convolve a random noise image to obtain an artificial 3-D microstructure that had approximately the same porosity and functional form of S_2 as did the 2-D image. There are other ways of operating directly on random images to produce artificial structures. These methods are not based on the actual formation processes of the real material, and they may not even use a real image in the convolution algorithm. They are, however, useful because they can be easily generated and often bear reasonable resemblances to real microstructures.

One method is to take a random white noise image, convolve it with some other function, and then threshold it to solid and pore phases to give the desired porosity. This has been done using a Gaussian convolution function and, remarkably, provided images that resembled thin sections of carbonate rock [111]. If the convolution function is the Laplacian of a Gaussian, the resulting images exhibit features of Vycor™ [111, 112]. The microstructures in Fig. 4 are from Gaussian convolutions of a white noise image.

A variation of the preceding method uses two thresholds, x_1 and x_2. All pixels with values of x, $0 < x < 1$, below x_1 and above x_2 are designated pores, and pixels with $x_1 < x < x_2$ are designated as solid. This algorithm turned out to generate images that resembled foam-like and aerogel-like structures [113, 114]. The conductivity of these structures has been computed along with the two- and three-point correlation functions and resulting three-point bounds, and showed reasonable agreement with experimental measurements [113, 115].

This kind of model shows that as long as the correlation functions are similar to the real materials, artificial image models can be used productively to understand other material properties.

1.5.3 Microstructure Development Models

It is desirable to generate porous microstructures based on actual physical and chemical processes. This is often very difficult because of the complexity of these processes. Natural materials such as sandstone are not made under a controlled laboratory environment, so our quantitative knowledge of the processes involved is weak. However, man-made materials such as concrete (5 billion tonnes per year worldwide) and ceramics (including bricks) and various gels are manufactured according to well-defined processes, so in principle, it should be possible to simulate these processes by a 3-D microstructure model. The success of the model is, in fact, a test of our understanding of the processes.

Consider the case of the porous material concrete. It is made up of cement, water, sand, and pebbles (aggregates). It is formed by the hydration of cement, the most common variant of which, known as portland cement, consists of mainly calcium silicates with minor amounts of aluminate, sulphate, and ferrite phases [116]. When water is mixed with the cement, the various phases of the cement undergo hydration reactions, each at a different rate and interacting with each other. The initial viscous mixture of liquid and particulates grows into a rigid solid that keeps increasing its strength as the hydration progresses, which can continue for months. The cement paste (cement plus water) turns into a solid matrix, in which the sand and pebbles are embedded.

The main geometrical feature that must be understood about concrete microstructure to be able to optimize concrete properties is the development of the cement paste microstructure during hydration, because the cement paste matrix governs the properties of concrete. This is a microstructure made up of unhydrated cement grains, reaction products, and water-filled pore space. The starting cement grains have an average size of about 20–50 μm, so that the length scale that initially characterizes the primary cement paste pores is of the order of micrometers. These pores do, however, become as small as a tenth of a micrometer as hydration progresses. There are smaller secondary pores present, called gel pores, inherent in the main reaction product, amorphous calcium silicate hydrate. Their diameters are of the order of tens of nanometers [78, 116], but we ignore them in considering the primary cement paste microstructure. Cement paste is thus a porous material whose solid phase is not uniform. This has a sensitive effect on many concrete properties such as elastic moduli and thermal conductivity.

Models have been made to simulate the evolution of the cement paste microstructure from a mixture of water and cement grains to the final hydrated product [55, 117, 118]. These models incorporate only some of the relevant cement chemistry and physics. The amounts and volume of reac-

tants and products are correctly handled. The randomness of the original multiphase composite cement particles is realistically taken into account by using 2-D scanning electron microscope digital images of real particles as a basis for constructing 3-D particles [118]. The randomness in the growth process and the topology of the various reaction products are also realistically simulated.

Figure 16 (right) shows an SEM micrograph of a real cement paste, compared to the model equivalent in Fig. 16 (left) [55, 117]. The gray scales indicate the different phases. The darkest gray pixels contain other minority phases, including gel pores, which are not shown. The pores are black. For calculating composite properties such as elastic moduli, the different phases in the solid framework must be identified, as they all have different elastic moduli. Color pictures that reveal more details of the various stages of cement hydration can be found in Refs. [117–119].

Properties that have been computed using the various methods described in Section 1.3 of this chapter include the connectivity of both the solid and pore phases of hydrated cement [55], diffusivity of the pore space [63], and how the cement paste matrix in concrete is modified by the nearby presence of aggregates [119, 120]. Comparison with experimental data has been quite favorable.

Another example of a microstructural development model has to do with the high-temperature sintering of powders into ceramics and metals. The powder particles change shape, and the powder compact densifies to minimize surface energy [121]. This process has been simulated by a cellular

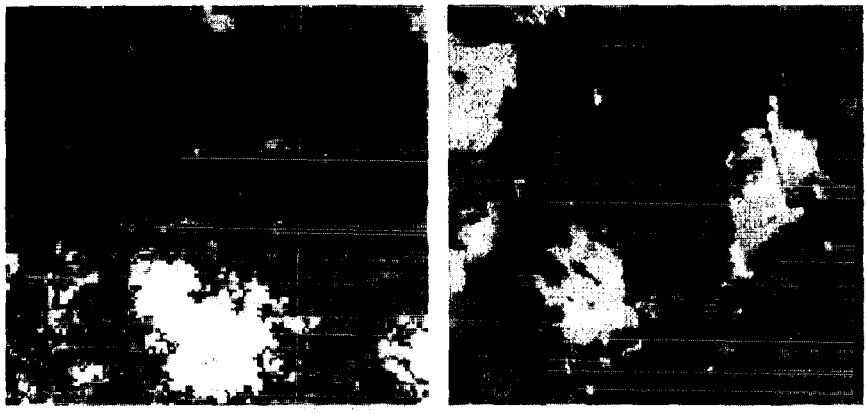

FIG. 16. A real hydrated cement paste (right) and its model equivalent (left). The different gray levels indicate the principal different solid phases of unhydrated cement and its reaction products. Porosity is black. The darkest gray level contains minor phases that are not shown.

automaton model that minimizes the surface area of a digital image of particles [122, 123]. A simple algorithm that transfers pixels from areas of high curvature to areas of low curvature captures the essence of the process. It is clear that by moving mountains to fill valleys, surface area is reduced, which is the main driving force for sintering. To implement the model on a digital image requires a simple algorithm to measure curvature, which is illustrated in Fig. 17. The solid pixels in this figure are shown with heavy black lines and the pore space pixels with thin black lines. A circular template (shown in gray) is centered at the point of interest on the surface. The local curvature is estimated by counting the number of pore pixels in the circular template. It is intuitively obvious that a flat surface would have 50% pore pixels in the circle, with less than 50% for negative curvature, and more than 50% for positive curvature. It can be proved mathematically [123] that this procedure is asymptotically exact, in the limit where the template radius is much smaller than the local radius of curvature. Other ways of measuring curvature in a digital image are described in Ref. [124]. The algorithm is applicable in three dimensions as well, but it gives only the average of the two principal radii of curvature [123].

Figure 18 shows the evolution (from left to right) of a collection of circular grains as the curvature and therefore surface area is reduced by the algorithm. The collection of grains is gradually becoming a circle, which has

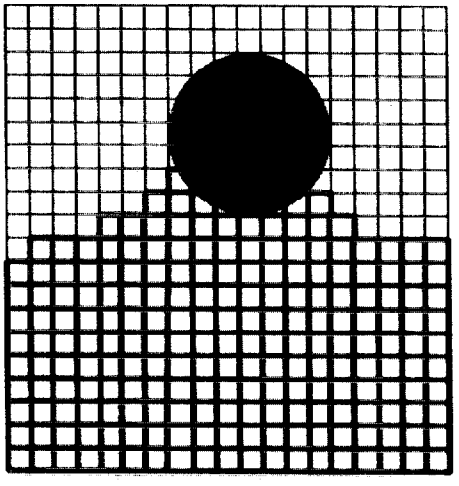

FIG. 17. The circular template algorithm in two dimensions. Thick black lines denote solid pixels, and thin black lines denote pore pixels. The circular template is shown in gray.

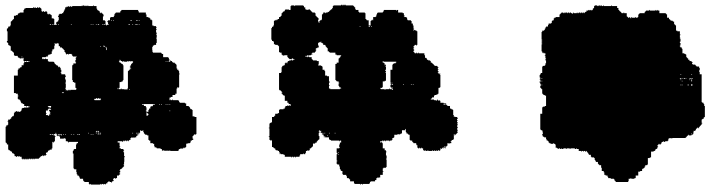

FIG. 18. The evolution of a collection of circular particles (left to right) under the sintering algorithm described in the text.

the minimum perimeter of a given surface area of any finite area shape in two dimensions [125]. This growth model can be applied directly to a digital image that has been acquired experimentally.

The sintering model described does not contain all of the relevant dynamics. When material is removed from a high-curvature surface, it must be transported to the low-curvature surface by either vapor transport through the pores, surface diffusion, volume diffusion, or diffusion through any grain boundaries. There are also elastic forces that arise from the tendency of the particles to coalesce to minimize surface area [126, 127].

1.5.4 Summary

With the rapid advance in computing and imaging tools, 2-D and 3-D digital images of porous materials can be readily obtained by a variety of techniques. Mathematical and computational techniques have been adapted to work with these images. In this chapter, we surveyed many of the techniques that have been applied to porous materials and showed the results. Although this is a rapidly advancing field, the essence is that a digital image converts a continuum picture into a lattice of discrete pixels, so that all lattice computational techniques are applicable.

The rapid growth of computing power will lead to more realistic models, and more 3-D experimental data, using x-ray tomography, nuclear magnetic resonance (NMR) imaging, and other methods. The improved characterization of pore geometry will result in more accurate calculation and prediction of material properties, which ultimately will aid in materials engineering via microstructural design.

Acknowledgments

We thank the NIST High-Performance Construction Materials and Systems program and the National Science Foundation Science and Tech-

nology Center for Advanced Cement-Based Materials for support of this work, M. F. Thorpe for useful conversations, and the NIST Scientific Visualization Group for help with many of the 3-D figures.

References

1. P. Hirsch, J. D. Birchall, D. D. Double, A. Kelly, G. K. Moir, and C. D. Pomeroy, *Phil. Trans. Roy. Soc. Lond.* **310**, 1–207 (1983).
2. S. Sapieha and P. Lepoutre, *Tappi* **65**, 99–101 (1982).
3. R. L. Coble and W. D. Kingery, *J. Am. Ceram. Soc.* **39**, 377–385 (1956).
4. J. Rodel and A. M. Glaeser, *J. Am. Ceram. Soc.* **70**, C172–C175 (1987).
5. R. L. Johnson, J. A. Cherry, and J. F. Pankow, *Environ. Sci. Technol.* **23**, 340–349 (1989).
6. R. L. Smith and S. D. Collins, *J. Appl. Phys.* **71**, R1–R2 (1992).
7. F. A. L. Dullien, *Porous Media: Fluid Transport and Pore Structure*, 2nd ed. (Academic Press, San Diego, 1992).
8. M. Sahimi, *Phys. Rev. A* **43**, 5367–5376 (1991).
9. M. Sahimi, *Flow and Transport in Porous Media and Fractured Rock* (VCH, New York, 1996).
10. M. A. Biot, *J. Appl. Phys.* **33**, 1482–1498 (1962); M. A. Biot, *J. Acoust. Soc. Am.* **34**, 1254–1264 (1962).
11. E. J. Garboczi, *Powder Tech.* **67**, 121–130 (1991). Also available at http://ciks.cbt.nist.gov/garboczi/, Chap. 11.
12. B. E. Hornby, L. M. Schwartz, and J. A. Hudson, *Geophysics* **59**, 1570–1583 (1994).
13. K. A. Snyder, E. J. Garboczi, and A. R. Day, *J. Appl. Phys.* **72**, 5948–5955 (1992).
14. C. Kittel, *Introduction to Solid State Physics*, 5th ed. (John Wiley & Sons, New York, 1979).
15. E. J. Garboczi, M. F. Thorpe, M. S. DeVries, and A. R. Day, *Phys. Rev. A* **43**, 6473–6482 (1991). Also available at http://ciks.cbt.nist.gov/garboczi/, Chap. 3.
16. N. Martys and E. J. Garboczi, *Phys. Rev. B* **46**, 6080–6090 (1992). Also available at http://ciks.cbt.nist.gov/garboczi/, Chap. 11.
17. J. Berryman, E. Garboczi, and N. Martys, unpublished.
18. B. Lu and S. Torquato, *J. Chem. Phys.* **93**, 3452–3459 (1990).
19. K. R. Castleman, *Digital Image Processing* (Prentice-Hall, Englewood Cliffs, NJ, 1981).
20. E. E. Underwood, *Quantitative Stereology* (Addison-Wesley, Reading, MA, 1970).

21. R. T. DeHoff and F. N. Rhines, *Quantitative Microscopy* (McGraw-Hill, New York, 1968).
22. John C. Russ, *The Image Processing Handbook* (CRC Press, Cleveland, OH, 1994).
23. V. Cantoni, S. Levialdi, and G. Musso, eds., *Image Analysis and Processing* (Plenum, New York, 1986).
24. J. Serra, *Image Analysis and Mathematical Morphology* (Academic Press, London, 1982); *Image Analysis and Mathematical Morphology Volume II: Theoretical Advances* (Academic Press, London, 1988).
25. B. B. Mandelbrot, *The Fractal Geometry of Nature* (W. H. Freeman, New York, 1983).
26. P. Wong, *Phys. Today* **41**, 24–25 (1988).
27. P. Wong, *Phys. Rev. B* **32**, 7417–7424 (1985).
28. P. Wong and A. J. Bray, *J. Appl. Cryst.* **21**, 786–794 (1988).
29. P. Wong and Q. Cao, *Phys. Rev. B* **45**, 7627–7632 (1992).
30. H. E. Stanley and N. Ostrowsky, eds., *Random Fluctuations and Pattern Growth* (Kluwer Academic, Dordrecht, 1988).
31. T. Vicsek, *Fractal Growth Phenomena* (World Scientific, Singapore, 1989).
32. F. Family and T. Vicsek, eds. , *Dynamics of Fractal Surfaces* (World Scientific, Singapore, 1991).
33. J. Feder, *Fractals* (Plenum, New York, 1988).
34. A. H. Thompson, A. J. Katz, and C. E. Krohn, *Adv. Phys.* **36**, 625–694 (1987).
35. D. W. Schaefer and K. D. Keefer, *Phys. Rev. Lett.* **56**, 2199–2202 (1986).
36. D. N. Winslow, J. M. Bukowski, and J. F. Young, *Cem. Conc. Res.* **25** (1), 147–156 (1995).
37. R. Lemaitre and P. M. Adler, *Transp. Porous Media* **5**, 325–340 (1990).
38. J. K. Williams and R. A. Dawe, *Transp. Porous Media* **1**, 201–209 (1986).
39. S. Torquato and G. Stell, *J. Chem. Phys.* **79**, 1505 (1983).
40. J. G. Berryman, *J. Appl. Phys.* **57**, 2374–2384 (1985).
41. P. Debye, H. R. Anderson, and H. Brumberger, *J. Appl. Phys.* **28**, 679 (1957).
42. J. G. Berryman, *J. Math. Phys.* **28**, 244–245 (1987).
43. J. G. Berryman and S. C. Blair, *J. Appl. Phys.* **60**, 1930–1938 (1986).
44. D. A. Coker and S. Torquato, *J. Appl. Phys.* **77**, 6087–6099 (1995).
45. D. A. Coker and S. Torquato, *J. Appl. Phys.* **77**, 955–964 (1995).
46. S. Torquato, *Appl. Mech. Rev.* **44**, 37–76 (1991).
47. Z. Hashin, *Appl. Mech.* **50**, 481–505 (1983).
48. W. F. Brown, *J. Chem. Phys.* **23**, 1514–1517 (1955).
49. S. Torquato, *J. Mech. Phys. Solids* **45**, 1421–1448 (1997).
50. J. G. Berryman and G. W. Milton, *J. Chem. Phys.* **83**, 754–760 (1985).
51. J. Rubinstein and S. Torquato, *J. Fluid Mech.* **206**, 25–46 (1989).

52. S. Torquato, *Phys. Rev. Lett.* **64**, 2644– 2646 (1990).

53. M. Avellaneda and S. Torquato, *Phys. Fluids A* **3**, 2529–2540 (1991).

54. D. Stauffer, *Percolation Theory* (Taylor and Francis, London, 1985).

55. D. P. Bentz and E. J. Garboczi, *Cem. Conc. Res.* **21**, 325–344 (1991). Also available at http://ciks.cbt.nist.gov/garboczi/, Chap. 5.

56. R. Zallen, *The Physics of Amorphous Solids* (John Wiley & Sons, New York, 1983), Chap. 4.

57. N. S. Martys, S. Torquato, and D. P. Bentz, *Phys. Rev. E* **50**, 403–408, 1994.

58. E. J. Garboczi, Finite element and finite difference programs for computing the linear electrical and elastic properties of digital images of random materials, National Institute of Standards and Technology Internal Report NISTIR 6269 (1999). Also available at http://ciks.cbt.nist.gov/garboczi/, Appendix 3.

59. M. J. Graf, C. A. Huber, T. E. Huber, and A. P. Salzberg, in *MRS Proc.* Vol. 195 *Physical Phenomena in Granular Materials*, edited by G. D. Cody, T. H. Geballe, and P. Sheng, pp. 397–402 (1991).

60. K. Kendall, *Powder Technol.* **62**, 1147–154 (1990).

61. C. B. Millikan, *Phil. Mag. S.* **7**, 641–662 (1929).

62. H. Helmholtz, *Wiss. Abh.* **1**, 223–230 (1868); J. B. Keller, L. A. Rubenfeld, and J. E. Molyneux, *J. Fluid Mech.* **30**, 97–125 (1967).

63. E. J. Garboczi and D. P. Bentz, *J. Mater. Sci.* **27**, 2083–2092 (1992). Also available at http://ciks.cbt.nist.gov/garboczi/, Chap. 5.

64. M. A. Ioannidis, M. J. Dwiecien, and I. Chatzis, *Transp. Porous Media* **29**, 61–83 (1997).

65. A. E. Scheidegger, *The Physics of Flow Through Porous Media* (University of Toronto Press, Toronto, 1974).

66. R. Peyret and T. D. Taylor, *Computational Methods for Fluid Flow* (Springer-Verlag, New York, 1983).

67. S. Whitaker, *Trans. Porous Media* **1**, 3 (1986).

68. D. L. Johnson, J. Koplik, and L. M. Schwartz, *Phys. Rev. Lett.* **57**, 2564 (1986).

69. A. J. Katz and A. H. Thompson, *Phys. Rev. B* **34**, 8179 (1986); *J. Geopys. Res.* **92**, 599 (1987).

70. L. D. Landau and E. M. Lifshitz, *Theory of Elasticity*, 3rd ed. (Pergamon Press, Oxford, 1986).

71. J. Poutet, D. Manzoni, F. Hage-Chehade, C. J. Jacquin, M. J. Bouoteca, J.-F. Thovert, and P. M. Adler, *Int. J. Rock Mech. Min. Sci. Geomech. Abstr.* **33**, 409–415 (1996); The effective mechanical properties of random porous media, *J. Phys. Mech. Solids* **44**, 1587–1620 (1996).

72. E. J. Garboczi and A. R. Day, *J. Phys. Mech. Solids* **43**, 1349–1362 (1995). Also available at http://ciks.cbt.nist.gov/garboczi/, Chap. 11.

73. R. D. Cook, D. S. Malkus, and M. E. Plesha, *Concepts and Applications of Finite Element Analysis*, 3rd ed. (John Wiley & Sons, New York, 1989).

74. S. P. Timoshenko and J. N. Goodier, *Theory of Elasticity*, 3rd ed. (McGraw-Hill Book Co., New York, 1970), 90–97.

75. E. J. Garboczi and D. P. Bentz, *Model. Sim. Mater. Sci. Eng.* **6**, 211–236 (1998). Also available at http://ciks.cbt.nist.gov/garboczi/, Chap. 11.

76. E. J. Garboczi and D. P. Bentz, *Ceram. Trans.* **16**, 365–379 (1991). Also available at http://ciks.cbt.nist.gov/garboczi/, Chap. 11.

77. J. A. Lewis, M. A. Galler, and D. P. Bentz, *J. Am. Ceram. Soc.* **79**, 1377–1388 (1996).

78. D. P. Bentz, D. A. Quenard, V. Baroghel-Bouny, E. J. Garboczi, and H. M. Jennings, *Mater. Struct.* **28**, 450–458 (1995). Also available at http://ciks.cbt.nist.gov/garboczi/, Chap. 4.

79. J. F. Thovert, J. Salles, and P. M. Adler, *J. Microsc.* **170**, 65–79 (1993).

80. D. A. Quenard, D. P. Bentz, and E. J. Garboczi, Capillary condensation, hysteresis, and image analysis, in *Drying 92*, A. S. Mudjumdar, ed. Pt. A, 252–262, (Elsevier Press, Amsterdam, 1992).

81. J. van Brakel, S. Modry, and M. Svata, *Powder Technol.* **29**, 1–12 (1981). This is the first article in a special issue devoted to mercury porosimetry.

82. D. H. Rothman, *Geophysics* **53**, 509 (1988); D. H. Rothman and S. Zaleski, *Rev. Mod. Phys.* **66**, 1417–1479 (1994).

83. N. S. Martys and H. Chen, *Phys. Rev. E* **53**, 743–750 (1996).

84. R. Benzi, S. Succi, and M. Vergassola, *Phys. Rep.* **222**, 145–197 (1992).

85. P. E. Stutzman, *Ceram. Trans.* **16**, 237 (1991).

86. B. P. Flannery, H. W. Deckman, W. G. Roberge, and K. L. D'Amico, *Science* **237**, 1439–1444 (1987).

87. D. P. Bentz, N. S. Martys, P. Stutzman, M. S. Levenson, E. J. Garboczi, J. Dunsmuir, and L. M. Schwartz, X-ray microtomography of an ASTM C-109 mortar exposed to sulfate attack, in *Microstructure of Cement-Based Systems/ Bonding and Interfaces in Cementitious Materials*, edited by S. Diamond et al. (Materials Research Society Vol. 370, Pittsburgh, 1995), pp. 77–82. Also available at http://ciks.cbt.nist.gov/garboczi/, Chap. 9.

88. F. M. Auzerais, J. Dunsmuir, B. B. Ferreol, N. Martys, J. Olson, T. S. Ramakrishman, D. H. Rothman, and L. M. Schwartz, *Geophys. Res. Lett.* **23**, 705–708 (1996).

89. M. Joshi, *A Class of Stochastic Models for Porous Media*, Ph.D. Thesis, Univ. of Kansas, 1974.

90. J. A. Quiblier, *J. Colloid Interf. Sci.* **98** 84–102 (1984).

91. P. M. Adler, C. G. Jacquin, and J. A. Quiblier, *Int. J. Multiphase Flow* **16**, 691–712 (1990).

92. P. M. Adler, C. G. Jacquin, and J. F. Thovert, *Wat. Res. Res.* **28**, 1571–1576 (1992).

93. D. P. Bentz and N. S. Martys, *Transp. Porous Media* **17**, 221–238 (1994).
94. D. A. Quenard, K. Xu, H. M. Kunzel, D. P. Bentz, and N. S. Martys, *Mater. Struct.* **31**, 317–324 (1998).
95. D. A. Young and E. M. Corey, *Phys. Rev. A* **41**, 7024–7032 (1990).
96. M. B. Isichenko, *Rev. Mod. Phys.* **64**, 961 (1992).
97. J. W. Essam, *Rep. Prog. Phys.* **43**, 833–912 (1980).
98. J. M. Hammersley and D. J. A. Welsh, *Contemp. Phys.* **21**, 593–605 (1980).
99. P. Renault, *Transp. Porous Media* **6**, 451–468 (1991).
100. S. Kirkpatrick, *Rev. Mod. Phys.* **45**, 574–588 (1973).
101. E. J. Garboczi, K. A. Snyder, J. F. Douglas, and M. F. Thorpe, *Phys. Rev. E* **52**, 819–828 (1995). Also available at http://ciks.cbt.nist.gov/garboczi/, Chap. 3.
102. W. Xia and M. F. Thorpe, *Phys. Rev. A* **38**, 2650–2655 (1988).
103. I. Balberg, *Phil. Mag. B* **56**, 991–1003 (1987).
104. P. Salatino and L. Massimilla, *Powder Technol.* **66**, 47–52 (1991).
105. M. Yanuka, *J. Coll. Inter. Sci.* **127**, 48–58 (1989).
106. L. M. Schwartz and S. Kimminau, *Geophysics* **52**, 1402–1411 (1987).
107. L. M. Schwartz, D. L. Johnson, and S. Feng, *Phys. Rev. Lett.* **52**, 831–834 (1984).
108. R. Lenormand, *Proc. Roy. Soc. London A* **423**, 159 (1989).
109. M. Blunt and P. King, *Phys. Rev. A* **42**, 4780–4787 (1990).
110. P. Wong, J. Koplik, and J. P. Tomanic, *Phys. Rev. B* **30**, 6066 (1984).
111. P. A. Crossley, L. M. Schwartz, and J. R. Banavar, *Appl. Phys. Lett.* **59**, 3553–3555 (1991).
112. R. Blumenfeld and S. Torquato, *Phys. Rev. E* **48**, 4492–4500 (1993).
113. A. P. Roberts and M. A. Knackstedt, *J. Mater. Sci. Lett.* **14**, 1357–1359 (1995).
114. A. P. Roberts and M. Teubner, *Phys. Rev. E* **51**, 4141–4154 (1995).
115. A. P. Roberts and M. A. Knackstedt, *Phys. Rev. E* **54**, 2313 (1996).
116. H. F. W. Taylor, *Cement Chemistry* (Academic Press, London, 1990).
117. D. P. Bentz, P. V. Coveney, E. J. Garboczi, M. F. Kleyn, and P. E. Stutzman, *Model. Simul. Mater. Sci. Eng.* **2**, 783–808 (1994).
118. D. P. Bentz, *J. Am. Ceram. Soc.* **80**, 3–21 (1997).
119. D. P. Bentz, E. Schlangen, and E. J. Garboczi, in *Materials Science of Concrete IV*, edited by J. Skalny and S. Mindess (American Ceramic Society, Westerville, Ohio, 1995).
120. D. P. Bentz, P. E. Stutzman, and E. J. Garboczi, *Cem. Conc. Res.* **22** (5), 891–902 (1992). Also available at http://ciks.cbt.nist.gov/garboczi/, Chap. 6.
121. W. D. Kingery, H. K. Bowen, and D. R. Uhlman, *Introduction to Ceramics*, 2nd ed. (John Wiley & Sons, New York, 1976).

122. P. Pimeinta, W. C. Carter, and E. J. Garboczi, *Comp. Mater. Sci.* **1**, 63–77 (1992). Also available at http://ciks.cbt.nist.gov/garboczi/, Chap. 10.

123. J. W. Bullard, E. J. Garboczi, W. C. Carter, and E. R. Fuller, *Comp. Mater. Sci.* **4**, 103–116 (1995). Also available at http://ciks.cbt.nist.gov/garboczi/, Chap. 10.

124. J. C. Russ, *J. Computer-Assisted Microsc.* **1**, 39–77 (1989).

125. G. Polya and G. Szego, *Isoperimetric Inequalities in Mathematical Physics* (Princeton University Press, Princeton, NJ, 1951).

126. J. W. Bullard and W. C. Carter, in *Sintering Technology*, edited by R. M. German, G. L. Messing, and R. G. Cornwall (Marcel Dekker, New York, 1996), 45–52.

127. J. W. Bullard, *J. Appl. Phys.* **81**, 159–168 (1997).